Comparison of Single Doppler and Multiple Doppler Wind Retrievals in Hurricane Matthew (2016)

Ting-Yu Cha[1] and Michael M. Bell[1]

[1]Department of Atmospheric Science, Colorado State University, Fort Collins, Colorado, United States

Correspondence: Ting-Yu Cha (tingyu@colostate.edu)

Abstract. Hurricane Matthew (2016) was observed by the ground-based polarimetric Next Generation Weather Radar (NEXRAD) in Miami (KAMX) and NOAA P-3 airborne tail Doppler radar near the coast of the southeastern United States for several hours, providing a novel opportunity to evaluate and compare single and multiple Doppler wind retrieval techniques for tropical cyclone flows. The generalized velocity track display (GVTD) technique can retrieve a subset of the wind field from a single ground-based Doppler radar under the assumption of nearly axisymmetric rotational wind, but is shown to have errors from aliasing of unresolved wind components. An improved technique that mitigates errors due to storm motion is derived in this study, although some spatial aliasing remains due to limited information content from the single Doppler measurements. A spline-based variational wind retrieval technique called SAMURAI can retrieve the full three-dimensional wind field from airborne radar fore-aft pseudo-dual Doppler scanning, but is shown to have errors due to temporal aliasing from the non-simultaneous Doppler measurements. A comparison between the two techniques shows that the axisymmetric tangential winds are generally comparable between the two techniques after the improvements to GVTD retrievals. Fourier decomposition of asymmetric kinematic and convective structure shows more discrepancies due to spatial and temporal aliasing in the retrievals. The strengths and weaknesses of each technique for studying tropical cyclone structure are discussed, and suggest that complementary information can be retrieved from both single and dual Doppler retrievals. Future improvements to the asymmetric flow assumptions in single Doppler analysis and steady-state assumptions in pseudo-dual Doppler analysis are required to reconcile differences in retrieved tropical cyclone structure.

1 Introduction

Doppler radar can provide high-resolution wind measurements within tropical cyclones (TCs), but the measurement is limited to the projection of the wind along the radial direction of the radar beam. Wind retrieval techniques are therefore required in order to identify the convective and kinematic structure of TCs from either single or multiple Doppler observations. While multiple Doppler retrievals are generally superior for deriving three-dimensional winds, measurements from two or more radars are not generally available and are often not simultaneous. In addition to the presence of two or more radars with sufficient range and geometry around the TC, a steady state assumption during the Doppler radar observation period is required. The steady state assumption is less severe for single Doppler wind retrievals, but more assumptions about the unresolved components of the flow are required. The strengths and weaknesses of different platform observing capabilities and retrieval techniques for TC

wind fields have not been compared and addressed fully. In this study, single Doppler and airborne dual Doppler observations simultaneously sampling Hurricane Matthew (2016) are analyzed to provide the first comprehensive comparison between the two wind retrieval techniques.

One of the primary dual-Doppler platforms for TC studies is the airborne National Oceanic and Atmospheric Administration
30   WP-3D (NOAA P-3) tail Doppler radar (TDR), which can obtain kinematic structure for storms well away from the U.S. coast. The TDR has been used since the early 1980's for airborne radar data collection in hurricane reconnaissance and research missions. In early usage, the wind field was reconstructed from using pseudo-dual Doppler analysis of two flight legs that were perpendicular to each other known as the "L" pattern (Marks and Houze, 1984, 1987). The "L" pattern takes a period of 0.5 to 1 hour to complete, such that some slowly evolving wind asymmetries can be deduced (Marks et al., 1992), but more rapidly
35   evolving structure cannot be retrieved by this technique.

In Lee et al. (1994), the Velocity Track Display (VTD) technique was proposed to retrieve the TC kinematic structure from a single airborne Doppler radar. The VTD technique takes advantage of the Doppler signatures of a vortex with a dipole pattern of approaching and receding velocities. The linear least squares method is utilized to fit Fourier basis functions onto the Doppler velocity, such that a subset of the wind field can be retrieved for each radius and altitude based on the Fourier
40   coefficients. VTD retrievals from Hurricane Gloria (1985) were compared with pseudo-dual Doppler analysis constructed from two orthogonal flight legs under the assumption that the circulation was in a steady state over 1-2 hour period. Lee et al. (1994) concluded that spatial and temporal aliasing in the pseudo-dual Doppler analysis over long periods tended to create artificial higher wavenumbers and reduce the wind maxima compared to the single Doppler retrievals. The study was one of the first to quantify the accuracy of low-wavenumber TC asymmetries from multiple Doppler analysis due to the evolving
45   weather.

The "Fore/Aft Scanning Technique" (FAST) was proposed by Hildebrand et al. (1986) in which the antenna alternately scans forward and then aft of the flight track within a few seconds. This scanning methodology can gather data faster, mitigating some of the impact from weather evolution, and no longer requires the execution an "L" shaped flight pattern. The FAST approach produces horizontal winds with high accuracy, and can yield vertical motion through the mass continuity equation or a multi-
50   beam technique with multiple aircraft (Jorgensen et al., 1996). The FAST scanning strategy has been used almost exclusively in recent years, and has provided significant advances of our understanding of TC structure and dynamics (Lee et al., 2003; Houze, 2010).

Although dual-Doppler observations can be used to assess snapshots of high resolution kinematic and convective structure, airborne reconnaissance and research missions are rare events in most of the countries impacted by TCs. The three-dimensional
55   airflow structure can also be retrieved from the dual-Doppler observations when the system is detected by two ground-based radars. Such dual-Doppler radar observations of TCs are usually limited by the radar range with only a small portion of TC (Jou et al., 1996) and extensive radar baselines. The range limitation can restrict the operational exploitation of dual Doppler measurements such that the wind retrieval based on single Doppler techniques is often required.

The Ground-based velocity track display (GBVTD) was developed by Lee et al. (1999) as an extension of VTD for stationary
60   radar scanning geometry. The GBVTD technique provides a new way to examine axisymmetric and asymmetric structures of a

TC near landfall from single ground-based Doppler radar, and has been successfully utilized in several studies (Lee et al., 2000; Lee and Bell, 2007; Zhao et al., 2008, 2012; Shimada et al., 2018). One limitation is that a ground-based Doppler radar has to be located outside of the radial distance between the radar and the storm center in order to sample the full tangential component of the vortex circulation accurately. Additionally, the GBVTD technique cannot fully separate the asymmetric components of the tangential and radial wind or the mean environmental wind due to spatial aliasing. Extensions to the GBVTD technique have been developed to better resolve asymmetries when multiple radars are available (EGBVTD) (Liou et al., 2006) or to resolve the mean wind when sufficient scatterers are near the radar (MGBVTD) (Chen et al., 2013).

The generalized velocity track display (GVTD) (Jou et al., 2008) is a technique that improves upon GBVTD by introducing an aspect ratio calculated by multiplying the distance of each gate (D) by measured Doppler velocity (V_d) and then scaling by the distance between the radar and the TC center (R_T). Key vortex kinematic structures displayed in the V_dD/R_T space simplify the interpretation of the radar signature and eliminate the geometric distortion inherited in the V_d space (Jou et al., 1996). GVTD expands V_dD/R_T into Fourier coefficients in a linear coordinate ($\theta^{'}$) rather than expanding V_d in a nonlinear coordinate ($\psi^{'}$) in GBVTD. The geometry and symbols of GVTD are displayed in Fig. 1. The retrieved wind field from GVTD is no longer limited by the analysis domain due to the required approximation of $\cos\alpha$ in GBVTD (Eq. (5) in Lee et al. (1999)), and the retrieved asymmetric structures are without distortion. Also, the GVTD formulation can be applied to the extensions of the velocity track display (VTD) techniques (e.g. GBVTD-simplex, Lee and Marks (2000)) to improve their performance. Therefore, it not only expands the capability of using ground-based Doppler radar data in TC forecasts but provides researchers an opportunity to examine TC kinematic and some derived dynamic variables in detail (such as vertical velocity, angular momentum, and vertical vorticity).

Jou et al. (2008) tested the GVTD technique with idealized vortices and confirmed that the modification by the aspect ratio is beneficial to retrieve the vortex kinematic structure. Although the GVTD technique largely improves and extends the capability of GBVTD, several limitations of the single-Doppler measurement remain. In particular, the equations are still underdetermined, and require a closure assumption in order to retrieve the asymmetric wind field.

The primary motivation of this study is to compare the strengths and weaknesses of the GVTD-technique and a dual-Doppler wind-synthesis analysis in a real case, which has not been done in previous studies. Hurricane Matthew (2016) was observed by the Next Generation Weather Radar (NEXRAD) radar in Miami (KAMX), concurrently with the NOAA P-3 (hereafter P3) airborne radar when it approached the southeastern United States. KAMX radar has a larger data coverage, but the P3 has better spatial resolution due to its closer range. Since airborne and ground-based radar collected data simultaneously, the case provides a unique opportunity to evaluate the wind retrievals. The datasets and methodology are described in section 2. The improved algorithm of the GVTD is formulated in section 3. In section 4, the improved GVTD algorithm is applied to the NEXRAD data in Hurricane Matthew (2016) and compared with the retrieved winds from the dual Doppler analysis. A summary of our results and conclusions are presented in section 5.

2   Datasets and methodology

Hurricane Matthew (2016) was the first Category 5 hurricane in the Atlantic basin since 2007, and caused widespread damage

95   across its destructive path. When Matthew moved parallel to the east coast of Florida, it was observed simultaneously by the KAMX single Doppler radar at a 5-minute interval and P3 TDR from 19 UTC 6 October to 00 UTC 7 October with four flight passes through the center during Matthew's eyewall replacement process.

The flight track of the P3 and the detecting range of KAMX radar are displayed in Fig. 2a. All radar sweep files were initially processed using an automated quality control (QC) script using National Center for Atmospheric Research (NCAR) SoloII

100   software (Bell et al., 2013) and then manually edited to unfold the Doppler velocity aliasing and remove the discontinuities and noise echoes. A coordinate transform and interpolation were applied to the KAMX radar fields from the original plan position indicators (PPIs) to the constant-altitude plan position indicators (CAPPIs) in Cartesian coordinates using Radx2Grid in the Lidar Radar Open Software Environment (LROSE) software (Bell, 2019). The gridded domain is 400 km × 400 km with a horizontal grid spacing of 1 km and vertical grid spacing of 0.5 km. The gridded data was further analyzed using the Vortex

105   Objective Radar Tracking and Circulation (VORTRAC) software in LROSE to obtain the kinematic structure by the improved GVTD algorithm formulated in section 3.1.

The P3 was involved in the reconnaissance mission from 19 UTC 6 October to 00 UTC 7 October. The P3 was equipped with the TDR, which scanned in FAST mode in order to obtain pseudo dual-Doppler measurements. The TDR documented the intensification and weakening stages of Matthew's ERC. The P3 flew four radial passes through the center of the TC, with

110   each pass being 30 to 60 minutes apart. The time window of the four passes are listed in Table 1, while the location of each pass is shown in Fig. 2a. The storm center and storm motion were both estimated from the Hurricane Research Division (HRD) aircraft-derived dynamic center (Willoughby and Chelmow, 1982). The analysis track for dual-Doppler analyses was linearly interpolated from each dynamic center using the derived storm motion. The dual-Doppler analysis was synthesized with each of the P3 radial passes at 1-km horizontal grid spacing and 0.5 km vertical grid spacing using SAMURAI software (Bell et al.,

115   2012) in LROSE. SAMURAI is a three-dimensional variational data assimilation tool that uses a finite element basis to estimate the most likely state of the atmosphere given a set of observations. The analysis was initially done on a Cartesian coordinate and then interpolated onto a cylindrical coordinate with azimuthal resolution of 1 degree and radial resolution of 1 km. The four passes were analyzed in detail to examine the changes in kinematic structure with high spatial resolution over four hours, with a particular focus on the first pass in this study.

120   3   The GVTD technique improvement

The Doppler velocity in Jou et al. (2008) is decomposed into tangential, radial, and mean wind components where storm motion is an implicit element in the mean wind component. The mean wind (V_M) is the horizontal average of the environmental flow at each altitude, which can be used to calculate the vertical wind shear. While the divergence of the environmental flow may not be zero since the environmental flow is not constant in the horizontal direction (Chan and Gray, 1982; Chan, 1984), we assume

125   a horizontally homogeneous mean wind in the following derivation. This assumption is different than the original derivation

in Jou et al. (2008) where the mean wind is a function of radius and height. Storm motion (U_S, V_S) is defined here as the deep layer motion vector over the whole vortex that varies only in time and does not vary with height or radius. The remaining terms in the GVTD formulation, namely the tangential (V_T)and radial (V_R) winds, are functions of radius, height and azimuth to the storm center. Despite the fact that the environmental wind is an important factor to determine storm motion, the storm motion

130   and environmental wind are not the same component due to vertical wind shear.

The storm motion and mean wind component were originally combined together in GVTD and affected the retrievals of the mean wind, and axisymmetric (wavenumber 0) tangential and radial winds. Notably, they do not have an influence on retrieving the phase and magnitude of GVTD-asymmetric components of tangential wind. However, when the storm moves fast or there is a high deviation of direction between mean wind and storm motion they can produce errors. To resolve this

135   error, we re-derive the GVTD technique and separate the storm motion from the mean wind component.

3.1   Mathematical formulation

Following the symbols and geometry utilized in the GBVTD (Lee et al., 1999) and GVTD (Jou et al., 2008) techniques, the addition of the storm motion to the geometry is illustrated in Fig. 1. We start with the horizontal projection of the Doppler velocity:

140   $$V_d/cos\phi = V_M cos(\theta_d - \theta_M) - V_T sin\psi + V_R cos\psi \tag{1}$$

where ϕ is the elevation angle of the radar, θ_d is the mathematical angle of the radar measured from the east, θ_M is the direction of mean wind, and ψ is the angle composed by the measured radar beam to the radar and the measured radar beam to the storm center. In this study, the storm motion (U_S, V_S) is added into the equation as an independent, known variable that projects onto the Doppler velocity, such that:

145   $$V_d/cos\phi = V_M cos(\theta_d - \theta_M) + U_S cos\theta_d + V_S sin\theta_d - V_T sin\psi + V_R cos\psi \tag{2}$$

where $\psi = \theta - \theta_d$. Rearranging Eq. 2, we obtain

$$
\begin{aligned}
V_d/cos\phi &= V_M cos(\theta_d - \theta_M) - V_T sin(\theta - \theta_d) + V_R cos(\theta - \theta_d) + U_S cos\theta_d + V_S sin\theta_d \\
&= V_M(cos\theta_d cos\theta_M + sin\theta_d sin\theta_M) - V_T(sin\theta cos\theta_d - cos\theta sin\theta_d) \\
&\quad + V_R(cos\theta cos\theta_d + sin\theta sin\theta_d) + U_S cos\theta_d + V_S sin\theta_d
\end{aligned}
\tag{3}
$$

The radar angle θ_d can be denoted as:

$$
\begin{aligned}
Dcos\theta_d &= Rcos\theta + R_T cos\theta \\
Dsin\theta_d &= Rsin\theta + R_T sin\theta
\end{aligned}
\tag{4}
$$

Atmospheric
Measurement
Techniques
Discussions

150   Plugging Eq. 4 into Eq. 3 and approximating $V_d/cos\phi$ with V_d at low elevation angles:

$$V_d = (-V_T sin\theta + V_R cos\theta + V_M cos\theta_M + U_S)(Rcos\theta + R_T cos\theta_T)/D$$

$$+ (V_T cos\theta + V_R sin\theta + V_M sin\theta_M + V_S)(Rsin\theta + R_T sin\theta_T)/D \quad (5)$$

Rearranging Eq. 5 and let $\theta' = \theta - \theta_T$, we obtain:

$$V_d \frac{D}{R_T} = [V_R \frac{R}{R_T} + V_M cos(\theta_T - \theta_M) + U_S cos\theta_T + V_S sin\theta_T]$$

$$- [V_T + \frac{R}{R_T}(V_M sin(\theta_T - \theta_M) + U_S sin\theta_T - V_S cos\theta_T)]sin\theta'$$

$$+ [V_R + \frac{R}{R_T}(V_M cos(\theta_T - \theta_M) + U_S cos\theta_T + V_S sin\theta_T)]cos\theta' \quad (6)$$

Decomposing $V_d D/R_T$, V_T, and V_R into Fourier components in the θ' coordinates:

$$V_d \frac{D}{R_T}(R, \theta') = A_0 + \Sigma A_n cosn\theta' + \Sigma B_n sinn\theta' \quad (7)$$

$$V_T(R, \theta') = V_T C_0 + \Sigma V_T C_n cosn\theta' + \Sigma V_T S_n sinn\theta' \quad (8)$$

$$V_R(R, \theta') = V_R C_0 + \Sigma V_R C_n cosn\theta' + \Sigma V_R S_n sinn\theta' \quad (9)$$

where A_n ($V_T C_n$ and $V_R C_n$) and B_n ($V_T S_n$ and $V_R S_n$) are the amplitude of the azimuthal wavenumber n cosine and sine components, as defined in Lee et al. (1999); Jou et al. (2008). Substituting Eqs. 7, 8, and 9 into Eq. 6, we obtain the following

160   expressions for the relation between the Fourier coeffients and wind components:

$$A_0 = \frac{R}{R_T}V_R C_0 + V_M cos(\theta_T - \theta_M) - \frac{1}{2}V_T S_1 + \frac{1}{2}V_R C_1 + U_S cos\theta_T + V_S sin\theta_T \quad (10)$$

$$A_1 = \frac{R}{R_T}V_R C_1 + \frac{R}{R_T}(V_M cos(\theta_T - \theta_M) + U_S cos\theta_T + V_S sin\theta_T) + V_R C_0 - \frac{1}{2}V_T S_2 + \frac{1}{2}V_R C_2 \quad (11)$$

$$B_1 = \frac{R}{R_T}V_R S_1 - \frac{R}{R_T}(V_M sin(\theta_T - \theta_M) + U_S sin\theta_T - V_S cos\theta_T) - V_T C_0 + \frac{1}{2}V_T C_2 + \frac{1}{2}V_R S_2 \quad (12)$$

$$A_n(n \geq 2) = \frac{R}{R_T} V_R C_n + \frac{1}{2}(V_T S_{n-1} + V_R C_{n-1} - V_T S_{n+1} + V_R C_{n+1}) \tag{13}$$

$$B_n(n \geq 2) = \frac{R}{R_T} V_R S_n + \frac{1}{2}(-V_T C_{n-1} + V_R S_{n-1} + V_T C_{n+1} + V_R S_{n+1}) \tag{14}$$

The Fourier coefficients can be rearranged to obtain each wind component of the vortex:

$$V_M \cos(\theta_T - \theta_M) = A_0 - \frac{R}{R_T} V_R C_0 + \frac{1}{2} V_T S_1 - \frac{1}{2} V_R C_1 - U_S \cos\theta_T - V_S \sin\theta_T \tag{15}$$

$$V_T C_0 = -B_1 - B_3 + \frac{R}{R_T}[-V_M \sin(\theta_T - \theta_M) + V_R S_1 + V_R S_3 - U_S \sin\theta_T + V_S \cos\theta_T] + V_R S_2 \tag{16}$$

$$V_R C_0 = \frac{A_0 + A_1 + A_2 + A_3 + A_4}{1 + \frac{R}{R_T}} - V_M \cos(\theta_T - \theta_M) - V_R C_1 - V_R C_2 - V_R C_3 - \frac{R}{R_T}(U_S \cos\theta_T + V_S \sin\theta_T) \tag{17}$$

$$V_T S_n = 2A_{n+1} - V_R C_n + V_T S_{n+2} - V_R C_{n+2} - 2\frac{R}{R_T} V_R C_{n+1} \tag{18}$$

$$V_T C_n = -2B_{n+1} + V_R S_n + V_T C_{n+2} + V_R S_{n+2} + 2\frac{R}{R_T} V_R S_{n+1} \tag{19}$$

Equations 15- 19 correspond to equations (16)-(20) in Jou et al. (2008) with the additional terms of storm motion on Eqs. 15- 17. The derivation shows that the storm motion is aliased on the components of mean wind, wavenumber 0 tangential and wavenumber 0 radial wind. Since the storm motion can be accurately estimated over successive radar volumes, the above equations can yield more accurate estimation of these wind components. However, the separation of storm motion and mean wind does not solve the underdetermined problem that the number of unknown variables is greater than the number of equations. We apply the same closure assumption in Lee et al. (1999) and Jou et al. (2008) that the asymmetric component of radial wind is much smaller than the asymmetric component of tangential wind, so the terms associated with radial wind asymmetries can be ignored. Future research is required to improve this closure assumption and retrieve the asymmetric radial wind.

With the above equations, the along-beam component of the mean flow, axisymmetric (n=0) tangential wind, axisymmetric radial wind, and asymmetric tangential winds (n=1-2) can be retrieved by performing linear least squares fit on $V_d D / R_T$ in a TC centered cylindrical coordinate. All data within 1-km radius-wide annulus are included in the linear least squares fit. To deal with missing data in observational radar data and reduce the influence of outliers, the truncation of the Fourier series follows Lee et al. (2000) (Table 2), which is consistent with the restriction of maximum allowable gap size in Lorsolo and Aksoy (2012). Lorsolo et al. have shown that the maximum allowable gap size varies with number of gaps and noise. If more gaps are present in the signal, the maximum allowable gap size is greater than originally suggested in Lee et al. (2000). We allowed the maximum wavenumber up to wavenumber 2 in the retrieved tangential wind in this study to reduce retrieval errors.

3.2 GVTD-simplex center finding

The GVTD algorithm can be highly sensitive to the center location. Jou et al. (2008) showed that the uncertainty of the center
190 location cannot exceed 5 km, or about 20% of the radius of the maximum wind (RMW), in order to have a reasonable wind
retrieval. There are several ways to identify TC center, such as the geometric center (Griffin et al., 1992), wind center (Wood
and Brown, 1992), dynamic center (Willoughby and Chelmow, 1982) and vorticity center (Marks et al., 1992). The centers
identified by different methods are not necessarily collocated, and the range of uncertainties is a few kilometers or more. Since
both vorticity centers estimated from the GVTD technique and dynamic centers derived from the aircraft reconnaissance were
195 available, the comparison of the different centers is required in order to have a better result of wind retrieval.

The GBVTD-simplex algorithm is a method to identify TC vorticity centers using single-Doppler radar data developed by
Lee and Marks (2000). The simplex center is found by maximizing the mean tangential wind within an axisymmetric TC with
three operations on a simplex: reflection, contraction, and expansion. The GBVTD-simplex algorithm reduces the uncertainties
in estimating TC position and improves the quality of the GBVTD-retrieved TC circulation. The deviation of the true centers to
200 the GBVTD-simplex center in an idealized TC is approximately 340 m. In this study, since the GVTD technique has better wind
field estimation, we conducted the GVTD-simplex method to estimate the centers following the GBVTD-simplex algorithm.
By maximizing GVTD-retrieved mean tangential wind, using the GVTD technique to estimate the TC vorticity center has
higher accuracy than the GBVTD technique.

The GVTD-simplex method is performed as the following procedure:
205 (1) Doppler velocities on a CAPPI were interpolated onto a cylindrical grid with 1-km radial spacing centered at a given TC
center.
(2) Find the TC center possessing the highest mean tangential wind within an axisymmetric TC.
(3) Use three operations on a simplex : reflection, contraction, and expansion - to search for a new maximum or minimum in
the field around the simplex. We put the dynamic center from HRD as the first guess. The operation process would start from
210 this point and find the circulation center.

To compare the performance of GVTD-simplex and GBVTD-simplex centers, the dynamic centers from HRD are treated
as the reference center because they are consistently centered at the geometric center of the storm over our analysis period
compared to the simplex centers. The continuous centers are interpolated from the dynamic centers with a series of spline
curves every two minutes. Figure 2b shows that the centers retrieved by the GVTD-simplex method are not consistent with that
215 of the retrievals from the GBVTD-simplex method, which is due to the more accurate estimation of axisymmetric tangential
wind. Although the GVTD-simplex centers follow more closely to the dynamic centers over the 35 hours of observation,
the location of the GVTD-simplex center is still variable, similar as GBVTD-simplex center (Lee and Marks, 2000) and not
consistent with different radar retrievals (such as KAMX vs. KMLB, and KMLB vs. KJAX). Since the GVTD technique is
highly sensitive to the storm center and the dynamic centers are qualitatively and quantitatively better than the simplex centers
220 in terms of consistency, our study utilized the dynamic centers to perform the GVTD technique.

4 Wind retrievals comparison between single Doppler and airborne dual Doppler analyses

4.1 Wavenumber 0 tangential wind retrieval

The dual Doppler analyses from the four aircraft passes into Hurricane Matthew are optimal to evaluate the performance of the GVTD technique because we can obtain all coefficients (Eqs. 15 to 19) from the Fourier decomposition of V_T and V_R,

225 known storm motion, and mean wind components, which ensures the comparability of the wind field. To evaluate the improved algorithm, the wind fields from the dual Doppler analyses were resampled into Doppler velocity that would be observed by KAMX radar. The wind fields were then retrieved from the resampled velocities using the original and improved GVTD algorithms (Table 1). Figure 3a and b show the Doppler velocity observed by KAMX radar and the Doppler velocity projected from dual Doppler analysis using the 1855 - 1940 UTC aircraft data as an example. Figure 3c and d show the reflectivity

230 field from KAMX radar observation and dual-Doppler analysis respectively. The single Doppler observations have much more missing data in the eye and the moat due to the reduced sensitivity to weak echoes at longer range from the radar. Additionally, the maximum Doppler velocity of single Doppler observations is not collocated with the maximum Doppler velocity of the resampled dual Doppler analysis. This discrepancy is believed to be due to temporal aliasing from the extended sampling period of the aircraft pass compared to the ground-based scanning. The issue of temporal aliasing of airborne Doppler analysis

235 will be discussed in more detail in section 4.2. Despite the aliasing, the dual Doppler analysis provides a relatively complete, consistent wind field and can reasonably be assumed as the "truth" for the purposes of algorithm evaluation.

Figure 4 displays the results from the improved GVTD algorithm compared to the original GVTD algorithm and the "true" wavenumber 0 (axisymmetric) tangential wind derived from the four dual-Doppler analyses. The green dashed line (hereafter optimal solution) shows the improved GVTD retrieved axisymmetric tangential wind (V_TC_0) when all the terms are known.

240 This optimal retrieval from the resampled V_dD/R_T from the dual Doppler analysis using Eq. 16 has the least deviation from the "truth" (black line) in general. When the storm motion is removed from the V_TC_0 retrieval (blue dashed line, hereafter optimal but without storm motion) the axisymmetric wind in the inner eyewall (between 10 and 30 km) does not differ significantly from the "truth". As the radius increases, the storm motion term becomes more important to the retrieval of wavenumber 0 tangential wind. Between the radius of 55 to 65 km the impact of neglecting the storm motion term can be up to $3\text{-}4\,\mathrm{m\,s^{-1}}$. In

245 the optimal retrieval, all terms in Eq. 16 are known, but in practice, the retrieved Fourier coefficients are underdetermined and a closure assumption is required to retrieve V_TC_0, typically by neglecting the cross-beam mean wind and asymmetric radial wind. The orange line (hereafter original GVTD) in Fig. 4 shows the result of the original GVTD algorithm invoking this closure assumption where only the B1 and B3 coefficients are used to retrieve V_TC_0. The red line (hereafter improved GVTD) shows the improvement to the GVTD algorithm by adding in the storm motion terms, while still invoking the necessary closure

250 assumption. The deviations from the "truth" caused by the closure assumption occur at different radii depending on the aircraft pass, suggesting that the neglected terms have different magnitudes in different parts of the storm. For example, in pass 1 the deviations are most pronounced from 55 - 70 km radius, while in pass 4 the deviations are most pronounced from 15 - 25 km radius.

Atmospheric
Measurement
Techniques
Discussions

Root-mean-square (RMS) differences of the above $V_T C_0$ solutions (optimal, optimal but without storm motion, original
GVTD and improved GVTD algorithms) averaged over the four passes are shown in Table 3. The optimal solution has the least
deviation from the "truth". Including the storm motion terms decreases the RMS differences about $0.8\,\mathrm{m\,s^{-1}}$ in both optimal
versus optimal without storm motion and improved GVTD versus original GVTD. Interestingly, RMS difference of improved
GVTD algorithm has a similar magnitude as the optimal solution but without storm motion, suggesting that the influence from
storm motion herein is similar as neglecting terms in Eq. 16.

255

The $V_T C_0$ retrieved by the original (orange dots) and improved (red dots) GVTD algorithm from the KAMX observations
alone (Fig. 3a) are also shown in Fig. 4. The axisymmetric tangential winds retrieved from KAMX alone are in generally good
agreement with the winds from the dual Doppler analyses. As in the dual Doppler retrieval, the storm motion term has relatively
small impact on the retrieval in the inner eyewall because R/R_T is small. The deviation between the retrievals becomes larger
beyond the radius of 40 km, but the improved GVTD algorithm is generally more consistent with the "truth" compared to the
original GVTD algorithm. RMS differences show a reduction $0.4\,\mathrm{m\,s^{-1}}$ between the original and improved GVTD algorithms
compared to the "truth" (Table 3). The comparison demonstrates that the inclusion of the storm motion has better consistency of
the wavenumber 0 tangential wind intensity with the dual-Doppler reference solution, and that the improved GVTD technique
can provide insightful information about TC kinematic structure from ground-based single Doppler radar data.

260

265

4.2 Asymmetric wind retrievals

270

Both Lee et al. (1999) and Jou et al. (2008) have tested the GBVTD and GVTD techniques respectively with analytic datasets
and confirmed the accuracy of these two methods. Murillo et al. (2011) further assessed the ability of GBVTD to retrieve low-
wavenumber wind structure by comparing simultaneous single Doppler and dual-Doppler retrievals in Hurricane Danny (1999)
using ground-based radar observations. However, no previous studies to the authors' knowledge have conducted a detailed
comparison of the Fourier decomposition of the wind field between single Doppler and airborne dual-Doppler wind retrievals.
We have already shown that wavenumber 0 tangential wind from the dual Doppler analyses can be accurately retrieved by the
GVTD-improved algorithm in section 4.1. With the confidence of the performance of the GVTD technique, the next step is to
examine the low-wavenumber structure and applicability of a steady-state assumption of the dual Doppler analysis.

275

Figure 5a displays $V_d D/R_T$ on a ring at the RMW (18 km) derived from the dual Doppler and single Doppler analyses. For
clarity, we use the term "harmonics" to refer to Fourier decomposition in $V_d D/R_T$ around the ring, and "wavenumbers" to refer
to the components of tangential wind which are constructed from combinations of the observed Doppler harmonics. $V_d D/R_T$
constructed from both analyses are dominated by a single harmonic pattern with very similar magnitude. Nevertheless, a small
difference of $V_d D/R_T$ pattern between the two analyses is evident. The discrepancies of the pattern and magnitude suggest
that higher harmonics of the $V_d D/R_T$ coefficients are different.

280

Figure 5b shows the residuals after the subtraction of harmonics 0 and 1 components from the total $V_d D/R_T$, with the
harmonic 2 components of $V_d D/R_T$ highlighted. The residuals include the harmonic 2 and higher components of $V_d D/R_T$.
The residuals from the single Doppler analysis (light red line) are dominated by a wavenumber 2 component, while the residuals
from the dual Doppler analysis (light green line) are without a clear pattern. The peak value of the residual from the single

285

Atmospheric
Measurement
Techniques
Discussions

Open Access

EGU

Doppler analysis is $8\,\mathrm{m\,s^{-1}}$, but the peak value of the residual from the dual Doppler analysis is about $3\,\mathrm{m\,s^{-1}}$. To quantitatively compare the two retrievals, Table 4 shows the retrieved magnitude of harmonics 0 - 3 around the RMW. The magnitude of

290 harmonics 0, 1, and 3 are similar at the RMW for the two analyses with around $1\,\mathrm{m\,s^{-1}}$ deviation. The similarity in harmonic 1 is primarily responsible for the similarity in the wavenumber 0 tangential wind (Fig. 4). Harmonic 2 shows a much larger deviation of $6\,\mathrm{m\,s^{-1}}$, resulting in different wavenumber 1 tangential wind retrievals.

Figure 6 shows the harmonics of $V_d D/R_T$ as a function of radius for the resampled dual Doppler wind field (green dashed line) and single Doppler observations (red dots). Note that the ordinate on each panel is different due to the varying magnitudes

295 of each coefficient. A_0, A_1 and B_1 coefficients are roughly consistent between the two analyses within the eyewall region (15 - 25 km) with small deviations less than $2\,\mathrm{m\,s^{-1}}$. The deviations in A_0, A_1 and B_1 coefficients are larger from the eye to the inner edge of the eyewall (10 - 15 km) and outside of the eyewall region (beyond 25 km), but generally have a similar magnitude. On the other hand, larger discrepancies are apparent with A_2 and B_2. A_2 is similar between 10 to 20 km, but has a large $7\,\mathrm{m\,s^{-1}}$ difference outside 20 km. B_2 is different at nearly all radii, with up to $7\,\mathrm{m\,s^{-1}}$ differences. The different amplitudes of A_2 and

300 B_2 indicate that the retrieved wavenumber 1 tangential wind phase and magnitude are inconsistent (Eq. 19). Discrepancies are also evident in the A_3 and B_3 coefficients, indicating inconsistencies in the retrieved wavenumber 2 tangential wind phase and magnitude as well.

We hypothesize that the discrepancies of retrieved wavenumber 1 and 2 tangential winds are due to the steady state assumption in the dual Doppler analysis. A steady state assumption is not applicable when the temporal evolution of the phenomena is

305 faster than the period of data collection. For example, the propagation velocity of a wavenumber 2 vortex Rossby wave (VRW) is half of the symmetric tangential wind velocity (Lamb, 1932; Guinn and Schubert, 1993; Kuo et al., 1999). A propagating wavenumber 2 asymmetry could then alias onto other wavenumbers, contributing to a discrepancy in wavenumber 1 tangential wind.

To test the hypothesis, the phases of maximum wavenumber 1 and wavenumber 2 tangential winds retrieved from the 5-

310 minute single Doppler observations are examined in Fig. 7 for the temporal evolution during the first flight pass from 1907 to 1940 UTC. The amplitude and phase (Eqs. 18 and 19) of wavenumber 1 and 2 tangential winds are denoted in polar coordinates by the radius and azimuth, respectively. The wavenumber 1 tangential wind (Fig. 7a) generally stayed unchanged throughout the first pass with a magnitude between 8 and $12\,\mathrm{m\,s^{-1}}$ and phase to the E to NE. Environmental vertical wind shear derived from the Statistical Hurricane Intensity Prediction Scheme dataset (SHIPS) points to the northeast direction with

315 a magnitude of $7\,\mathrm{m\,s^{-1}}$, suggesting that the wavenumber 1 distribution is forced by the vertical wind shear to be consistently in the downshear-right quadrant.

The wavenumber 2 tangential wind (Fig. 7b) propagated cyclonically during the flight pass with a magnitude up to $7\,\mathrm{m\,s^{-1}}$. The propagation of the wavenumber 2 tangential wind is estimated to be 285 degrees from 1907 to 1940 UTC, which is $35\,\mathrm{m\,s^{-1}}$, or 63% of V_{Tmax}. The propagation of the wavenumber 2 tangential wind is roughly consistent with linear VRW

320 theory (Kuo et al., 1999; Cha et al., in review).

According to the single Doppler analysis, the wavenumber 2 VRW propagated approximately 43 degrees every five minutes on average. The wavenumber 2 maximum amplitudes were located in the NE and SW quadrants as the P3 approached the inner

eyewall from the SW (Fig. 2), such that the TDR would see the maximum component in the SW eyewall. The VRW rotated cyclonically as the P3 crossed the 36 km diameter eye at $120\,\mathrm{m\,s^{-1}}$, such that by the time the P3 exited the eyewall the radar

325 would begin to see the wavenumber 2 wind minimum on the NE side. The SW maximum and NE minimum would then appear as a wavenumber 1 component under a steady state assumption. The analysis supports our hypothesis that the propagation of wavenumber 2 tangential wind is aliased onto the steady wavenumber 1 component, resulting in a reduced amplitude and a phase shift in A_2 and B_2 in the dual Doppler analysis.

The above analysis suggests that both the dual Doppler and single Doppler analysis have strengths and weaknesses. The

330 retrieved wavenumber 0 component of tangential wind has been shown to be comparable between an airborne dual Doppler wind synthesis and single Doppler retrieval due to the fact that a steady state assumption for one flight pass is usually valid to apply to the axisymmetric circulation. The axisymmetric kinematic structure of Hurricane Matthew revealed in the dual Doppler analysis is consistent with the single Doppler retrievals across multiple aircraft passes (Cha, 2018). However, the steady-state assumption is not applicable with more rapidly evolving features, such as convective bursts, rotation of mesovor-

335 tices, and propagation of a wavenumber 2 or higher VRWs. The evolution during the aircraft pass could potentially impact the asymmetric reflectivity and wind structure retrieval from a dual or multi-Doppler analysis due to temporal aliasing. On the other hand, dual Doppler analysis can retrieve high-quality and detailed three-dimensional structure, whereas a ground-based single Doppler radar retrieval is often limited by spatial aliasing and the observing distance from the radar to TC. Nevertheless, the analyses presented herein demonstrate that complementary information can be retrieved from both single and dual Doppler

340 retrievals.

5 Conclusions

Tropical cyclone (TC) wind retrieval techniques from Doppler radar observations are salient to identify the convective and kinematic structure and evolution of TCs. Previous studies have used the ground-based velocity track display (GBVTD) (Lee et al., 1999; Lee and Marks, 2000; Lee and Bell, 2007; Zhao et al., 2008) or the generalized velocity track display (GVTD)

345 (Jou et al., 2008; Cha et al., in review) techniques from single Doppler observations, and airborne dual-Doppler analysis (Bell et al., 2012; Cha, 2018) to analyze TC intensity evolution, but no previous studies to the authors' knowledge have conducted a detailed comparison of the wind field between single Doppler and airborne dual-Doppler wind retrievals. Hurricane Matthew (2016) was observed by the polarimetric Next Generation Weather Radar (NEXRAD) in Miami (KAMX) and NOAA P-3 airborne radar near the coast of Florida for several hours, providing a novel opportunity to evaluate and compare single and

350 dual Doppler wind retrieval techniques for TC flows.

Jou et al. (2008) has shown that the GVTD technique improves the capability of the GBVTD and can retrieve a subset of the wind field from a single ground-based Doppler radar under the assumption of nearly axisymmetric rotational wind. Here we present an improved technique that mitigates errors due to storm motion, which yields a more accurate estimation of mean wind, wavenumber 0 tangential and radial winds. The aliasing of unresolved wind components from the single Doppler measurements

355 remains, so another closure assumption for the GVTD technique is needed to improve the accuracy of the retrieval. In addition

to the wind improvements, the GVTD-simplex centers follow more closely to the dynamic centers compared to GBVTD-simplex centers due to the more accurate estimation of axisymmetric tangential wind. However, the GVTD-simplex centers are still varying and not fully consistent with different radar (such as KAMX vs. KMLB, and KMLB vs. KJAX). The dynamic centers herein are shown to be qualitatively and quantitatively better than the simplex center. Nevertheless, the improvement of

360   TC wind estimation presented herein can be useful in deducing storm structure for research purposes and assimilating real-time TC intensity and structure for forecasts (Zhao et al., 2012).

The strengths and weaknesses of different platform observing capabilities and retrieval techniques for TC wind fields are discussed in this study. The full three-dimensional wind field from airborne radar fore-aft pseudo-dual Doppler scanning can be retrieved by a spline-based technique called SAMURAI, but is shown to have errors due to temporal aliasing from the non-

365   simultaneous Doppler measurements when the temporal evolution of the phenomena is faster than the period of data collection. Single Doppler wind retrieval by the GVTD technique can be obtained at a 5-minute interval, but spatial aliasing remains due to the limited measurements from only radial direction of the radar beam. A comparison between the two techniques shows that the retrieved axisymmetric (wavenumber 0) component of tangential winds are generally comparable between the two techniques after the improvements to GVTD retrievals, due to the fact that a steady state assumption for one flight pass

370   (30-60 minutes) is usually valid to apply to the axisymmetric circulation. Fourier decomposition of asymmetric kinematic and convective structure shows more discrepancies between the two techniques due to spatial and temporal aliasing in the retrievals. The propagation of wavenumber 2 tangential wind is found to be aliased onto the steady wavenumber 1 component retrieved by the dual Doppler analysis, causing a reduced amplitude and phase shift of wavenumber 1 tangential wind. The steady-state assumption for low-wavenumber structure retrievals from pseudo-dual Doppler analysis is not applicable with the presence

375   of rapidly evolving features, and the temporal evolution within one flight pass should be considered. On the other hand, the steady-state assumption is less severe for single Doppler wind retrievals, and the rapidly evolving phenomena, such as vortex Rossby waves, have been documented by several studies using the single Doppler observations (Corbosiero et al., 2006; Cha et al., in review). The analyses presented herein demonstrate that complementary information can be retrieved from both single and dual Doppler retrievals. Future work on the time-dependent analysis of asymmetric structure in dual Doppler retrieval and

380   asymmetric flow closure assumptions in single Doppler retrieval are required to reconcile differences in retrieved TC structure.

Code and data availability. The underlying Julia code is available from the author upon request. The data used in this paper are available through zenodo: http://doi.org/10.5281/zenodo.3899262. The Vortex Objective Radar Tracking And Circulation (VORTRAC) and SAMURAI software are open source and available on the web: http://lrose.net.

Author contributions. The study was designed by both authors. TC carried out the analysis and made the figures supervised by MB. TC

385   wrote the manuscript with contributions from MB.

Competing interests. The authors declare that they have no conflict of interest.

Atmospheric
Measurement
Techniques
Discussions

References

Bell, M. M.: nsf-lrose/lrose-blaze: lrose-blaze-20190105, https://doi.org/10.5281/zenodo.2532758, 2019.

390   Bell, M. M., Montgomery, M. T., and Lee, W.-C.: An axisymmetric view of concentric eyewall evolution in Hurricane Rita (2005), J. Atmos. Sci., 69, 2414–2432, https://doi.org/10.1175/JAS-D-11-0167.1, 2012.

Bell, M. M., Lee, W.-C., Wolff, C. A., and Cai, H.: A Solo-based automated quality control algorithm for airborne tail Doppler radar data, J. Appl. Meteor. Climatol., 52, 2509–2528, https://doi.org/10.1175/JAMC-D-12-0283.1, 2013.

Cha, T.-Y.: Eyewall Replacement Cycle of Hurricane Matthew (2016) observed by Doppler radars, M. S. Thesis, p. Colorado State University, 395   2018.

Cha, T.-Y., Bell, M. M., Lee, W.-C., and DesRosiers, A. J.: Polygonal eyewall asymmetries during the rapid intensification of Hurricane Michael (2018), Geophys. Res. Lett., in review.

Chan, J. C.: An observational study of the physical processes responsible for tropical cyclone motion, J. Atmos. Sci., 41, 1036–1048, https://doi.org/10.1175/1520-0469(1984)041<1036:AOSOTP>2.0.CO;2, 1984.

400   Chan, J. C. and Gray, W. M.: Tropical cyclone movement and surrounding flow relationships, Mon. Wea. Rev., 110, 1354–1374, https://doi.org/10.1175/1520-0493(1982)110<1354:TCMASF>2.0.CO;2, 1982.

Chen, X., Zhao, K., Lee, W.-C., Jong-Dao Jou, B., Xue, M., and Harasti, P. R.: The Improvement to the Environmental Wind and Tropical Cyclone Circulation Retrievals with the Modified GBVTD (MGBVTD) Technique, J. Appl. Meteor. Climatol., 52, 2493–2508, https://doi.org/10.1175/JAMC-D-13-031.1, 2013.

405   Corbosiero, K. L., Molinari, J., Aiyyer, A. R., and Black, M. L.: The structure and evolution of Hurricane Elena (1985). Part II: Convective asymmetries and evidence for vortex Rossby waves, Mon. Wea. Rev., 134, 3073–3091, https://doi.org/10.1175/MWR3250.1, 2006.

Griffin, J. S., Burpee, R. W., Marks, F. D., and Franklin, J. L.: Real-time airborne analysis of aircraft data supporting operational hurricane forecasting, Wea. Forecasting, 7, 480–490, https://doi.org/10.1175/1520-0434(1992)007<0480:RTAAOA>2.0.CO;2, 1992.

Guinn, T. A. and Schubert, W. H.: Hurricane Spiral Bands, Journal of the Atmospheric Sciences, 50, 3380–3403, 410   https://doi.org/10.1175/1520-0469(1993)050<3380:HSB>2.0.CO;2, 1993.

Hildebrand, P. H., Walther, C., and Frush, C.: The NCAR Electra Doppler radar, in: Part I: Evaluation of scientific needs. Preprints, 23rd Conf. on Radar Meteorology, Snowmass, CO, Amer. Meteor. Soc, pp. 147–150, 1986.

Houze, Robert A., J.: Clouds in Tropical Cyclones, Mon. Wea. Rev., 138, 293–344, https://doi.org/10.1175/2009MWR2989.1, 2010.

Jorgensen, D., Matejka, T., and DuGranrut, J.: Multi-beam techniques for deriving wind fields from airborne Doppler radars, Meteor. Atmos. 415   Phys., 59, 83–104, https://doi.org/10.1007/BF01032002, 1996.

Jou, B. J.-D., Deng, S.-M., and Chang, B.: Determination of typhoon center and radius of maximum wind by using Doppler radar, Atmos. Sci, 24, 1–24, 1996.

Jou, B. J.-D., Lee, W.-C., Liu, S.-P., and Kao, Y.-C.: Generalized VTD retrieval of atmospheric vortex kinematic structure. Part I: Formulation and error analysis, Mon. Wea. Rev., 136, 995–1012, https://doi.org/10.1175/2007MWR2116.1, 2008.

420   Kuo, H.-C., Williams, R., and Chen, J.-H.: A possible mechanism for the eye rotation of Typhoon Herb, J. Atmos. Sci., 56, 1659–1673, https://doi.org/10.1175/1520-0469(1999)056<1659:APMFTE>2.0.CO;2, 1999.

Lamb, H.: Hydrodynamics, Cambridge university press, 1932.

Lee, W.-C. and Bell, M. M.: Rapid intensification, eyewall contraction, and breakdown of Hurricane Charley (2004) near landfall, Geophys. Res. Lett., 34, https://doi.org/10.1029/2006GL027889, 2007.

425 Lee, W.-C. and Marks, F. D.: Tropical cyclone kinematic structure retrieved from single-Doppler radar observations. Part II: The GBVTD-simplex center finding algorithm, Mon. Wea. Rev., 128, 1925–1936, https://doi.org/10.1175/1520-0493(2000)128<1925:TCKSRF>2.0.CO;2, 2000.

Lee, W.-C., Marks, F. D., and Carbone, R. E.: Velocity track display—A technique to extract real-time tropical cyclone circulations using a single airborne Doppler radar, J. Atmos. Oceanic Technol., 11, 337–356, https://doi.org/10.1175/1520-
430 0426(1994)011<0337:VTDTTE>2.0.CO;2, 1994.

Lee, W.-C., Jou, B. J.-D., Chang, P.-L., and Deng, S.-M.: Tropical cyclone kinematic structure retrieved from single-Doppler radar observations. Part I: Interpretation of Doppler velocity patterns and the GBVTD technique, Mon. Wea. Rev., 127, 2419–2439, https://doi.org/10.1175/1520-0493(1999)127<2419:TCKSRF>2.0.CO;2, 1999.

Lee, W.-C., Jou, B. J.-D., Chang, P.-L., and Marks, F. D.: Tropical cyclone kinematic structure retrieved from single-Doppler radar ob-
435 servations. Part III: Evolution and structures of Typhoon Alex (1987), Mon. Wea. Rev., 128, 3982–4001, https://doi.org/10.1175/1520-0493(2000)129<3982:TCKSRF>2.0.CO;2, 2000.

Lee, W.-C., Marks, F. D., and Walther, C.: Airborne Doppler radar data analysis workshop, Bull. Amer. Meteor. Soc., 84, 1063–1075, 2003.

Liou, Y.-C., Wang, T.-C. C., Lee, W.-C., and Chang, Y.-J.: The retrieval of asymmetric tropical cyclone structures using Doppler radar simulations and observations with the extended GBVTD technique, Mon. Wea. Rev., 134, 1140–1160, https://doi.org/10.1175/MWR3107.1,
440 2006.

Lorsolo, S. and Aksoy, A.: Wavenumber analysis of azimuthally distributed data: Assessing maximum allowable gap size, Mon. Wea. Rev., 140, 1945–1956, https://doi.org/10.1175/MWR-D-11-00219.1, 2012.

Marks, F. D. and Houze, R. A.: Airborne Doppler Radar Observations in Hurricane Debby, Bull. Amer. Meteor. Soc., 65, 569–582, https://doi.org/10.1175/1520-0477(1984)065<0569:ADROIH>2.0.CO;2, 1984.

445 Marks, F. D. and Houze, R. A.: Inner Core Structure of Hurricane Alicia from Airborne Doppler Radar Observations, J. Atmos. Sci., 44, 1296–1317, https://doi.org/10.1175/1520-0469(1987)044<1296:ICSOHA>2.0.CO;2, 1987.

Marks, F. D., Houze, R. A., and Gamache, J. F.: Dual-aircraft investigation of the inner core of Hurricane Norbert. Part I: Kinematic structure, J. Atmos. Sci., 49, 919–942, https://doi.org/10.1175/1520-0469(1992)049<0919:DAIOTI>2.0.CO;2, 1992.

Murillo, S. T., Lee, W.-C., Bell, M. M., Barnes, G. M., Marks, F. D., and Dodge, P. P.: Intercomparison of Ground-Based Velocity Track
450 Display (GBVTD)-Retrieved Circulation Centers and Structures of Hurricane Danny (1997) from Two Coastal WSR-88Ds, Monthly Weather Review, 139, 153–174, https://doi.org/10.1175/2010MWR3036.1, 2011.

Shimada, U., Sawada, M., and Yamada, H.: Doppler Radar Analysis of the Rapid Intensification of Typhoon Goni (2015) after Eyewall Replacement, J. Atmos. Sci., 75, 143–162, https://doi.org/10.1175/JAS-D-17-0042.1, 2018.

Willoughby, H. E. and Chelmow, M. B.: Objective determination of hurricane tracks from aircraft observations, Mon. Wea. Rev., 110,
455 1298–1305, https://doi.org/10.1175/1520-0493(1982)110<1298:ODOHTF>2.0.CO;2, 1982.

Wood, V. T. and Brown, R. A.: Effects of radar proximity on single-Doppler velocity signatures of axisymmetric rotation and divergence, Mon. Wea. Rev., 120, 2798–2807, https://doi.org/10.1175/1520-0493(1992)120<2798:EORPOS>2.0.CO;2, 1992.

Zhao, K., Lee, W.-C., and Jou, B. J.-D.: Single Doppler radar observation of the concentric eyewall in Typhoon Saomai, 2006, near landfall, Geophys. Res. Lett., 35, https://doi.org/10.1029/2007GL032773, 2008.

460 Zhao, K., Xue, M., and Lee, W.-C.: Assimilation of GBVTD-retrieved winds from single-Doppler radar for short-term forecasting of super typhoon Saomai (0608) at landfall, Quart. J. Roy. Meteor. Soc., 138, 1055–1071, https://doi.org/10.1002/qj.975, 2012.
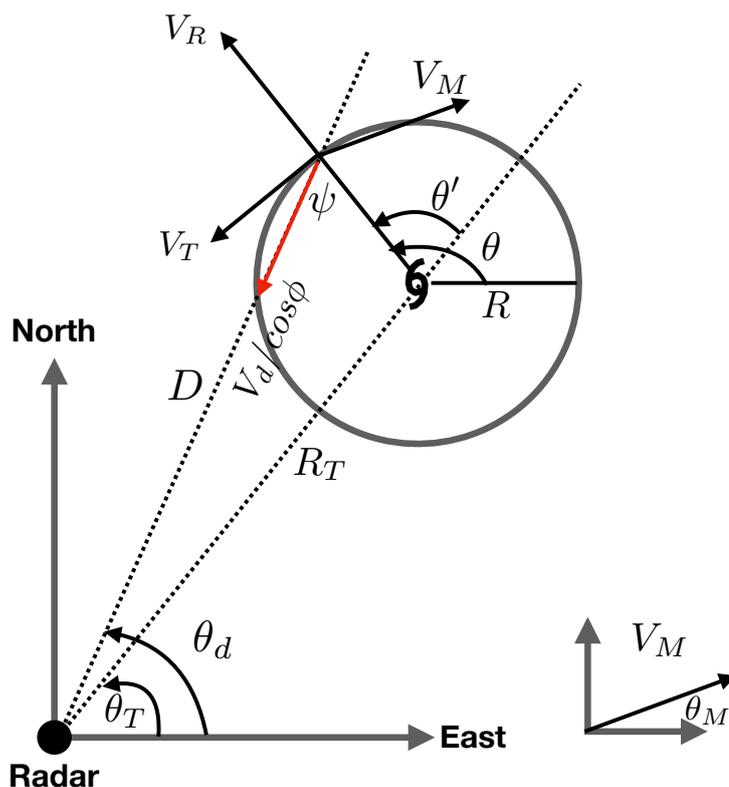
Figure 1. The geometry and symbols used in the formulation of GVTD (modified from Jou et al. (2008)). Red arrow denotes the Doppler velocity.

Table 1. Details of aircraft missions and corresponded KAMX ground-based radar observation period for this study.

Radar analysis	Duration
P3	1855-1940 UTC 6 Oct 2016
P3	2020-2105 UTC 6 Oct 2016
P3	2145-2230 UTC 6 Oct 2016
P3	2305-2340 UTC 6 Oct 2016
KAMX	1907-0550 UTC 6-7 Oct 2016
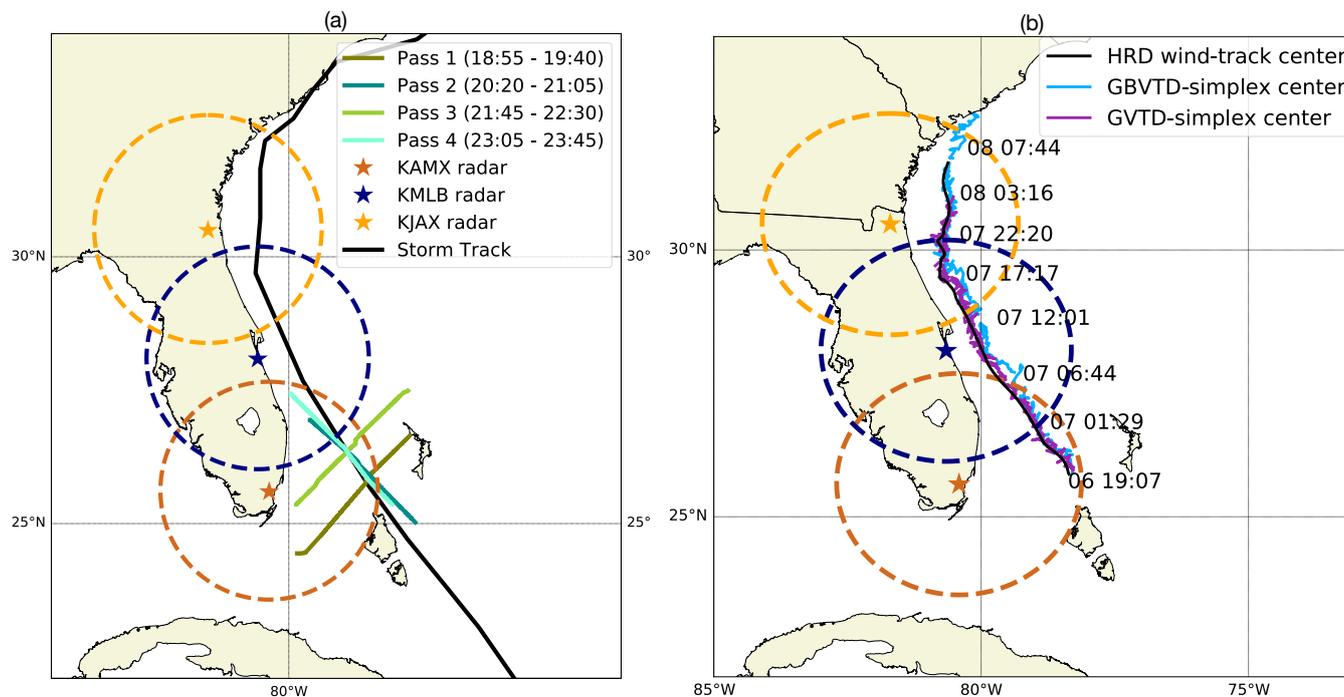
Figure 2. (a) Hurricane Matthew's storm track from best track data (black line) and the deployed observation instruments. Pass 1-4 denote the passage of P-3 plane across the cyclone on 6 October. Colored circles and stars represent the ground-based radar detecting range (230 km) and location of single Doppler radar respectively. (b) Comparison of Hurricane Matthew's track between HRD dynamic center (black line), GBVTD-simplex center (light blue line), and GVTD-simplex center (purple line). Colored circles and stars are the same as (a).

Table 2. The maximum allowable data gap determines the maximum wavenumber used in the least squares fit.

Wavenumber	Gap(^{o})
0	≤ 180
1	≤ 90
2	≤ 60

Table 3. The averaged root mean squared error of the $V_T C_0$ retrieved from different methods described in Fig. 4 from four flight passes and single Doppler radar observations. The errors are calculated from r = 10 - 70 km on z = 4 km.

Errors	P-3 dual-Doppler				NEXRAD single Doppler	
	Optimal	Optimal but no storm motion	Origial GVTD	Improved GVTD	Origial GVTD	Improved GVTD
RMSE (m s^{-1})	1.49	2.37	3.17	2.3	2.81	2.46
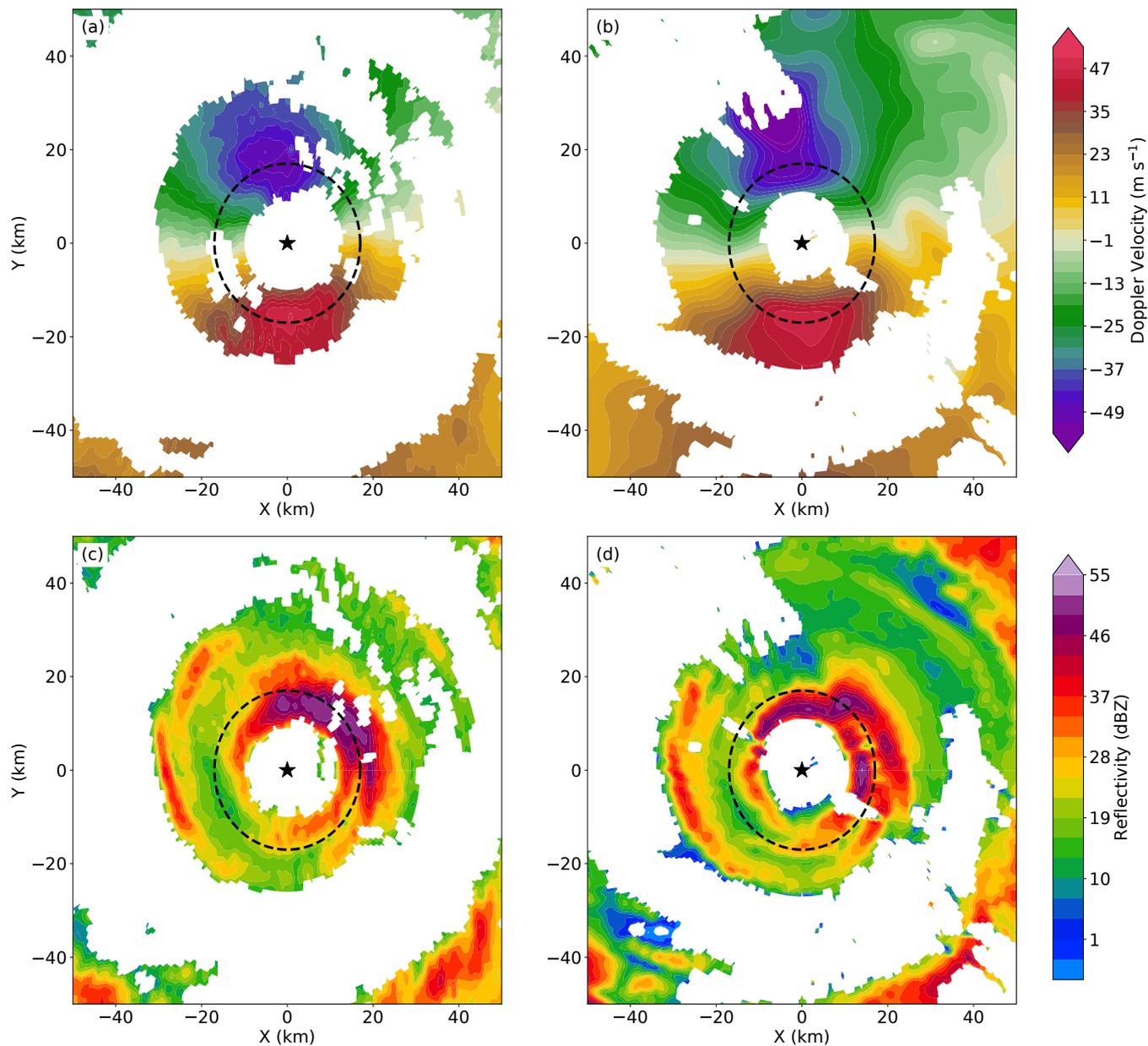
Figure 3. Doppler velocity at z = 4 km (a) observed by KAMX radar at 1921 UTC, and (b) resampled from dual Doppler analysis synthesized from 1855 - 1940 UTC. The black star denotes KAMX radar location, and the dashed circle denotes the radius of maximum wind of 18 km.
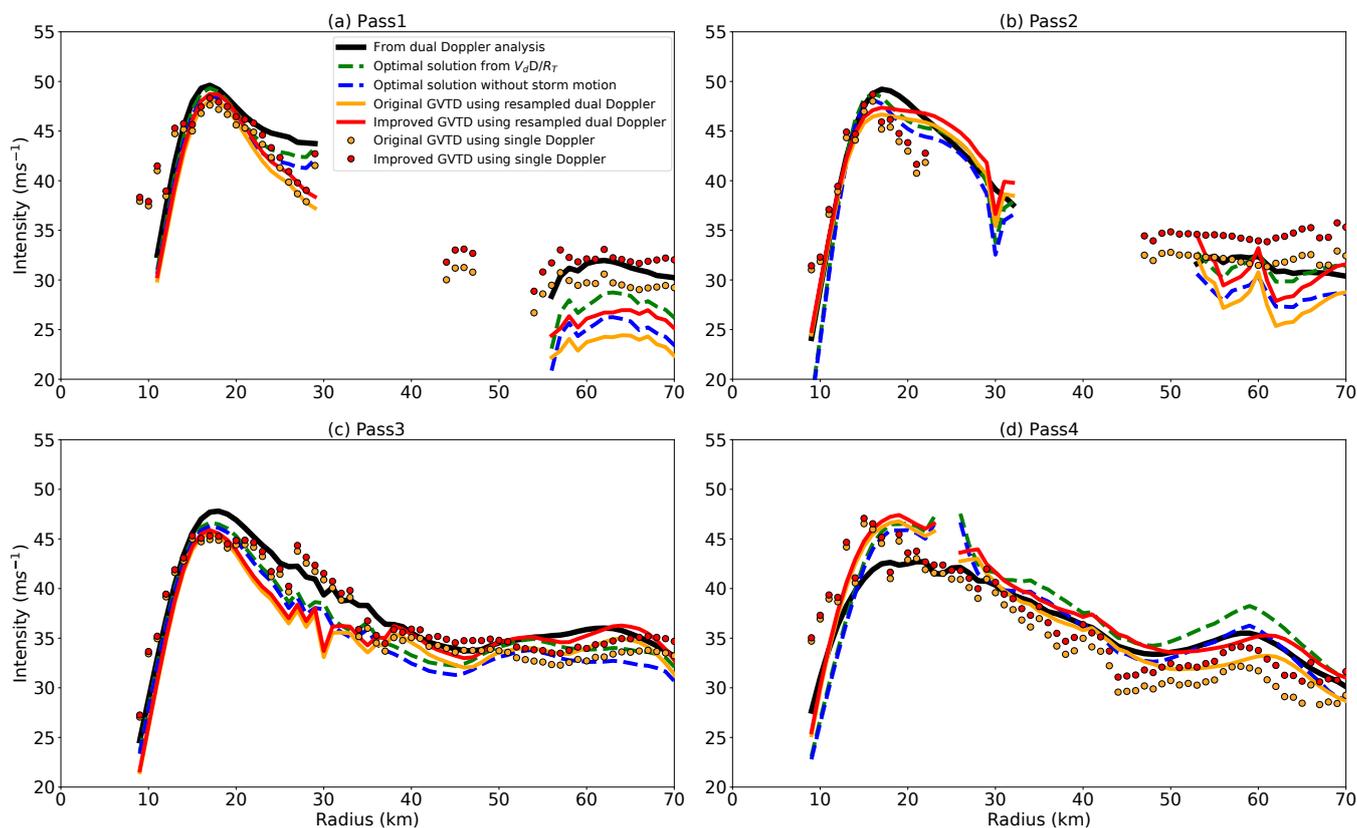
Figure 4. Wavenumber 0 tangential wind retrieved by the Fourier decomposition of tangential wind from the dual Doppler analysis (black line), the Fourier decomposition of $V_d D / R_T$ (green dashed line), the Fourier decomposition of $V_d D / R_T$ without storm motion (blue dashed line), the original GVTD algorithm (orange line), the improved GVTD algorithm (red line) from the dual Doppler analysis. Wavenumber 0 tangential wind retrieved by the single Doppler analysis from the original GVTD algorithm (orange dot), and improved GVTD algorithm (red dot). (a) Pass 1 from 1855 to 1940 UTC, (b) Pass 2 from 2020 to 2105 UTC, (c) Pass 3 from 2145 to 2230 UTC, (d) Pass 4 from 2305 to 2340 UTC.

Table 4. The Fourier coefficient magnitude of wavenumber 0, wavenumber 1 and wavenumber 2 retrieved by the single Doppler and dual Doppler analyses.

Coefficient magnitude (m s^{-1})	Single Doppler retrieval	Dual Doppler retrieval
A_0	0.26	-1.08
$\sqrt{A_1{}^2 + B_1{}^2}$	46.29	47.61
$\sqrt{A_2{}^2 + B_2{}^2}$	7.05	0.93
$\sqrt{A_3{}^2 + B_3{}^2}$	0.67	0.19
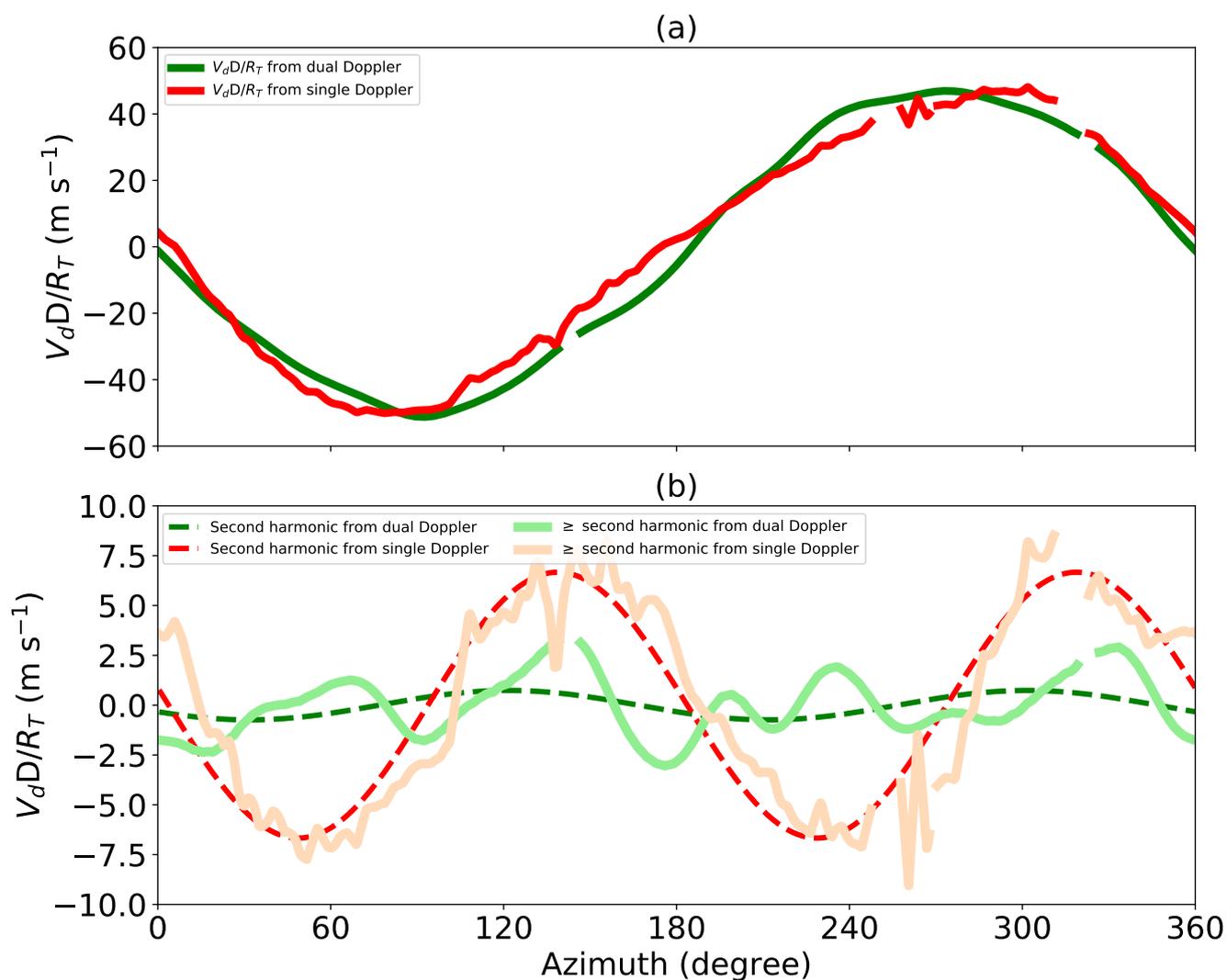
Figure 5. (a) Comparison of retrieved $V_d D/R_T$ between dual Doppler and single Doppler analyses at the RMW of 18 km. Green line denotes retrieved $V_d D/R_T$ from dual Doppler analysis synthesized from 1855 - 1940 UTC, and red line denotes retrieved $V_d D/R_T$ from KAMX radar at 1921 UTC. (b) Comparison of retrieved equal or greater than second harmonic components of $V_d D/R_T$ between dual Doppler and single Doppler analyses at the RMW. The solid line denotes the residuals of subtracting the harmonics 0 and 1 from $V_d D/R_T$. The dashed line represents the harmonic 2 of $V_d D/R_T$.
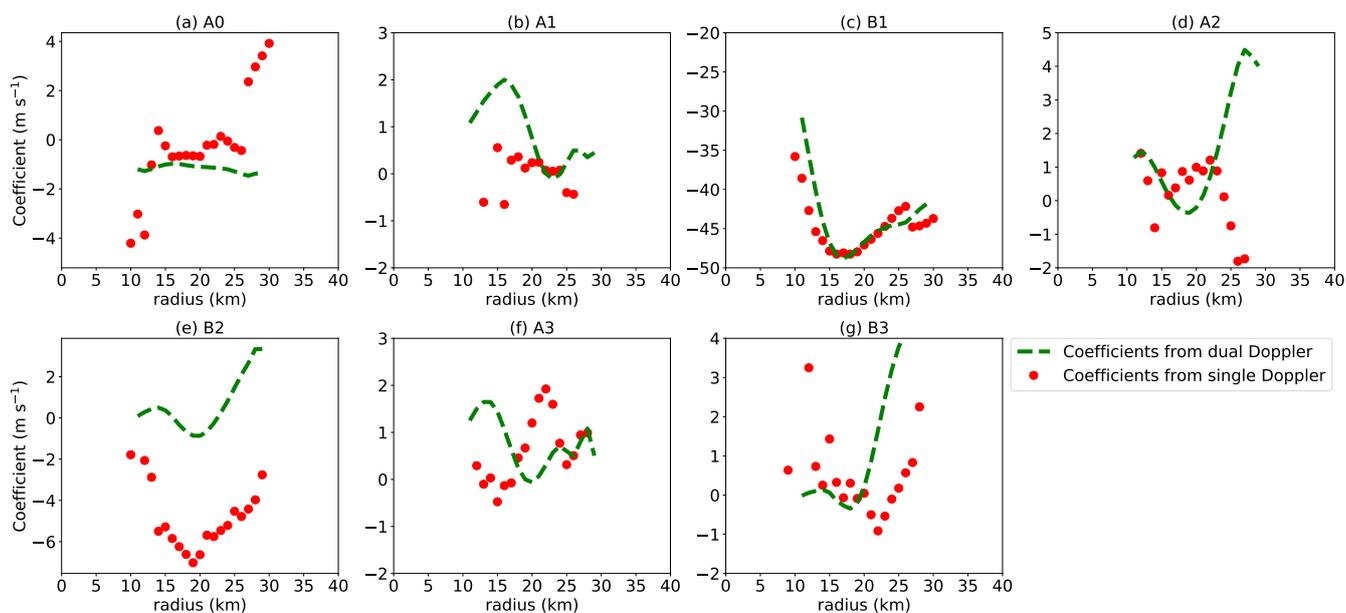
Figure 6. Comparison of $V_d D/R_T$ harmonics coefficients derived from the resampled Doppler velocity of dual Doppler analysis synthesized from 1855 - 1940 UTC using the improved GVTD technique (green dashed line), and single Doppler retrieval at 1921 UTC using the improved GVTD technique (red dot).
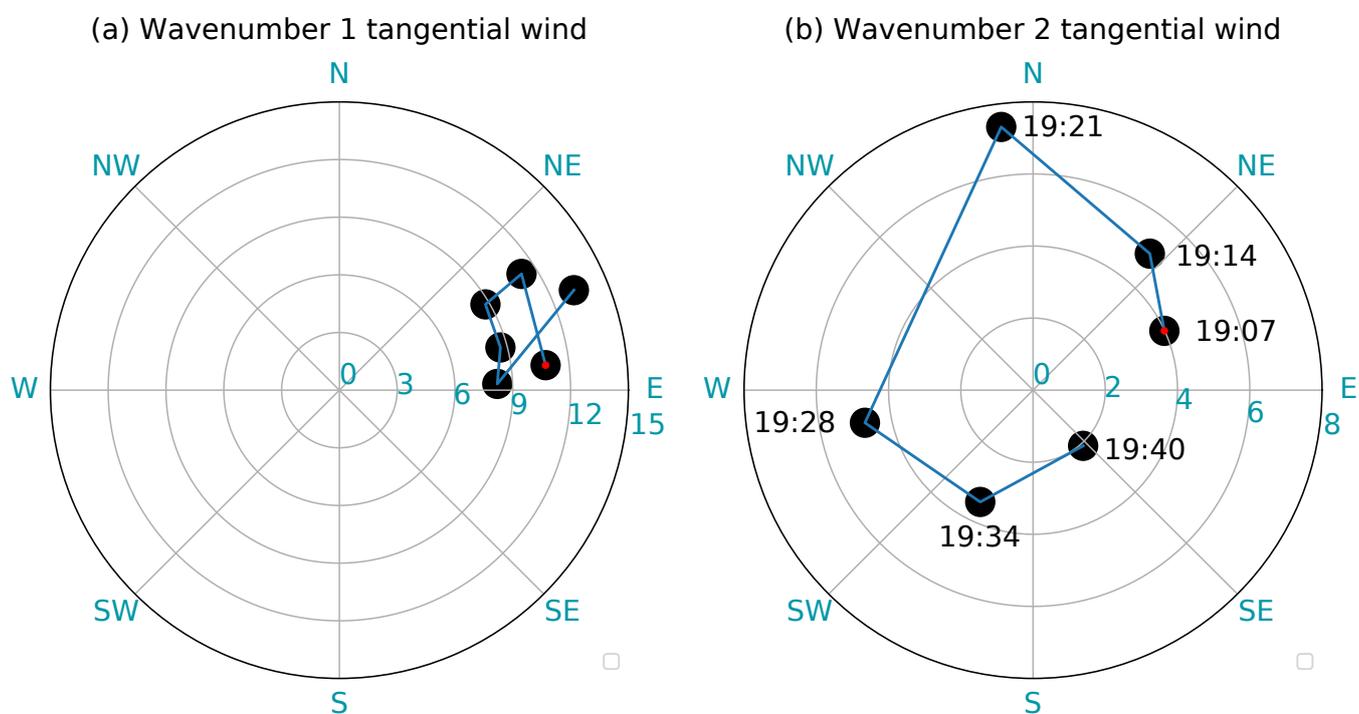
Figure 7. Azimuth and amplitude polar diagram of the temporal evolution of (a) maximum wavenumber 1 tangential wind amplitude and phase and (b) maximum wavenumber 2 tangential wind amplitude and phase in the inner eyewall (<18 km) derived from the GVTD single Doppler analysis from 1907 to 1940 UTC 6 October. The amplitude of the tangential wind component is denoted by the radius of each dot, with the phase denoted by the azimuth. The red dot in (a) and (b) indicates the starting time at 1907 UTC, and the temporal evolution follows the blue line.